Thionation of a Fluorescent Thieno[3,4-d]pyrimidine Derivative for the Development of a Heavy-Atom-Free Photosensitizer

Luis A. Ortiz-Rodríguez,[1,#] Ye-Guang Fang,[3,#] Germain Niogret, Kaivin Hadidi, Yitzhak Tor,[2,*] Ganglong Cui,[3,*] Carlos E. Crespo-Hernández[1,*]

[1] Department of Chemistry, Case Western Reserve University, Cleveland, OH, USA 44106

[2] Department of Chemistry and Biochemistry, University of California, San Diego, La Jolla, CA, USA 92093

[3] Key Lab of Theoretical and Computational Photochemistry, Ministry of Education, Chemistry College, Beijing Normal University, Beijing, 100875, China

Abstract

All-organic, heavy-atom-free photosensitizers based on thionation of nucleobases are receiving increased attention because they are easy to make, noncytotoxic, work both in the presence and absence of molecular oxygen and can be readily incorporated into DNA and RNA. In this contribution, the DNA and RNA fluorescent probe, thieno[3,4-d]pyrimidin-4(1H)-one, has been thionated to develop thieno[3,4-d]pyrimidin-4(1H)-thione, which is nonfluorescent and absorbs near-visible radiation with about 60% higher efficiency. Steady-state absorption and emission spectra are combined with transient absorption spectroscopy and CASPT2 calculations to delineate the electronic relaxation mechanisms of both pyrimidine derivatives in aqueous and acetonitrile solutions and to explain the origin of the remarkable fluorescence quenching in the thionated compound. It is demonstrated that thieno[3,4-d]pyrimidin-4(1H)-thione efficiently populates the long-lived and reactive triplet state in hundreds of femtoseconds independent of solvent. Conversely, fluorescence emission in thieno[3,4-d]pyrimidin-4(1H)-one is highly sensitive to solvent, with an order of magnitude decrease in fluorescence yield in going from aqueous to acetonitrile solution. Collectively, the experimental and computational results demonstrate that thieno[3,4-d]pyrimidine-4(1H)-thione stands out as the most promising thiopyrimidine photosensitizer developed to this date, which can be readily incorporated as a photodynamic agent into sequence-specific DNA and RNA sequences for the treatment of skin cancer cells.

1. Introduction

Photodynamic therapy (PDT) has grown in popularity in dermatology primarily because the effortless accessibility of the skin to light exposure and its simplicity of use.[1-3] PDT uses a photoactivable drug (a.k.a., photosensitizer) to generate singlet oxygen and other reactive oxygen species, offering a high degree of spatiotemporal selectivity in tumor destruction, noninvasiveness, and reduced side effects.[4-5] However, the development of highly effective photosensitizers has been a major challenge for the community because of difficulties in predicting a priori their intersystem crossing mechanisms, yield of triplet state population, and singlet oxygen generation efficacy. Furthermore, the efficacy of a photosensitizer depends not only on the type of target cells and their oxygenation status, but also its ability to penetrate the targeted diseased tissue selectively, and the wavelength of light activation.[6-7]

Transition metals and other heavy atoms have been introduced effectively into organic chromophores as a versatile strategy to yield photosensitizers for PDT,[8-11] but the dark toxicity of the heavy-atom-containing molecule continues to be a major concern. In this context, heavy-atom-free photosensitizers are emerging as an innovative class of photosensitizers exhibiting great potential for preclinical and clinical studies for the photodynamic treatment of cancers. Furthermore, heavy-atom-free photosensitizers (HAFPs) are receiving increased attention not only for PDT,[12-27] but also for photovoltaic,[28] and photocatalytic[29-30] applications, as well as for the development of innovative photonic technologies.[31-33] Some of the advantages of HAFPs over traditional photosensitizers include the high yield of triplet state population and the efficient generation of reactive oxygen species, low dark toxicity, long-lived excited triplet states, good photostability and biocompatibility, straightforward synthetic modification, and low cost.[16, 19]

Most HAFPs developed for PDT so far, however, do not only exhibit low water solubility and poor tumor selectivity, but also aggregate in aqueous media due to their hydrophobic and rigid structures.[19, 34-35] More broadly, the efficacy of most photosensitizers in preclinical and clinical use depends strictly on the molecular oxygen concentration available in solid tumors, which varies widely by location due to the aggressive proliferation of cancer cells and insufficient blood supply. Indeed, some interior regions of the tumor can exhibit molecular oxygen concentrations of less than 4%, decreasing up to 0% locally, which severely limits the efficacy of PDT against *in vivo* hypoxic tumors. Besides, because the PDT process itself consumes molecular oxygen, thereby effecting tumor hypoxia, the treatment itself can increase the tumor's resistance to PDT.[36-37] Clearly, the existing approaches have drawbacks and there is a clinical need to develop water-soluble and nonaggregating photosensitizer alternatives that offer improved target cell selectivity and the ability to photosensitize damage through more than one mechanism besides reactive oxygen species generation. Such HAFPs promise great prospect for improving tumor imaging and phototherapeutic efficacy.

In this context, site-selected sulfur-substituted nucleobases (a.k.a., thiobases) are emerging as a promising class of heavy-atom-free organic biomolecules for preclinical and clinical PDT applications.[13-14, 16, 38-42] The unique structural, biochemical, and photochemical properties of thiobases offer an attractive strategy for developing highly effective and highly targeted phototherapeutic compounds,[15, 43] which can be site-selectively incorporated into DNA and RNA sequences, working both in the absence and in presence of molecular

oxygen.[13, 15, 42, 44] A single-atom-substitution from oxygen to sulfur, converts DNA and RNA nucleobases into effective UVA chromophores ($\varepsilon \geq 10^4$ M^{-1} cm^{-1}) that exhibit red-shifted absorption maxima from ca. 320 to 380 nm, and with absorption bands extending all the way to the near visible region. These compounds have also been demonstrated to exhibit near-unity triplet yields and high yields of singlet oxygen generation,[15, 43] with one of most attractive applications being for the treatment of skin malignancies that are readily accessible to near-visible irradiation.[13, 39-42]

Similarly, thieno[3,4-d]pyrimidine derivatives can be easily incorporated into DNA,[45-47] and thionation of their carbonyl group would be expected to redshift their absorption spectra and to increase their triplet state population yields,[18, 21] thus generating reactive oxygen species including singlet oxygen. Therefore, to provide experimental confirmation of this idea, we have herein initially focused our efforts at demonstrating that thionation of the fluorescent thieno[3,4-d]pyrimidin-4(1H)-one (ThiaHX) at the C4 position (equivalent to the C6 position in the parent purine derivatives; see comment regarding the nomenclature used in Scheme 1), to generate thieno[3,4-d]pyrimidine-4(1H)-thione (ThiathioHX), should enable the development of a new class of highly effective all-organic HAF-PSs for further PDT implementation. In this contribution, we report a comprehensive characterization of the photophysical, photochemical, and electronic-structure properties of ThiaHX and ThiathioHX both in phosphate buffer solution at pH 7.4 and in acetonitrile studied by steady-state absorption and emission spectroscopies and femtosecond-broadband transient absorption measurements. The experimental results are enhanced with complete active space second-order perturbational theory (CASPT2) and time-dependent density functional (TDDFT) calculations. Detailed excited state deactivation mechanisms are presented for both molecules. Furthermore, unequivocal evidence is presented for the efficient population of the triplet state in ThiathioHX, revealing its great potential as a heavy-atom-free PDT agent and paving the way for further development of photosensitizers based on the thionation of thieno[3,4-d]pyrimidine derivatives.

2. Methods

2.1 Experimental Methods

Materials and Steady-State Measurements

The synthesis, as well as analytical (mass spectrometry, ^1H and ^{13}C-NMR) and crystal structure data for ThiaHX and ThiathioHX (structures in Scheme 1) are provided in the SI. Phosphate buffered solution (PBS) was freshly prepared using 0.2996 (± 0.0001) g of monobasic sodium phosphate and 0.2314 (± 0.0001) of dibasic sodium phosphate dissolved in 250 mL of ultrapure water and adjusted to pH 7.4 using a concentrated sodium hydroxide (NaOH) solution, with a total phosphate concentration of 16 mM. Phosphate salts and NaOH were purchased from Fischer Scientific, Inc. Acetonitrile (MeCN) was purchased from Fischer Scientific, Inc. Steady-state absorption and emission spectroscopy were performed using a Cary 300 and Cary Eclipse spectrometers, respectively. Fluorescence spectra were taken at PMT voltage of 800 V for ThiathioHX in PBS pH 7.4 and MeCN, 600 V for ThiaHX in MeCN and 400 V for ThiaHX in PBS pH 7.4 with slit widths of 5 nm and scan rate of 20 nm min^{-1}. Relative fluorescence quantum yields were obtained by using Tryptophan as a

standard.

Broadband transient absorption spectroscopy

Femtosecond transient absorption spectroscopy (fs-TAS) was used to study the excited-state dynamics of ThiaHX and ThiathioHX. The setup is described in detail in previous publications.[48-50] Briefly, a Ti:Spapphire oscillator (Vitesse, Coherent, Santa Clara, CA, USA) seed a regenerative amplifier (Coherent Libra-HE) that generates a 100 fs pulses at 800 nm with a repetition rate of 1 kHz is used to pump a Traveling Optical Parametric Amplifier of Superfluorescence (TOPAS, Quantronix/Light Conversion, Vilnius, Lithuania). In this work, the TOPAS was tuned to 325 and 385 nm. A translating 2 mm CaF_2 crystal was used to generate the white light continuum for probing (ca. 320 to 700 nm). The setup employs a mechanical delay stage with a physical temporal limit of 3 ns. The excitation pulses were set to a power of 1.75 mW (measured at the optical cell position) using a neutral density filter. A 2 mm optical cell was used. The solution was continuously stirred with a Teflon-coated magnetic stirrer. All solutions were kept below 10 % degradation, as judged from the absorption spectra taken at 308 and 367 nm before and after irradiation with the laser for ThiaHX and ThiathioHX, respectively. Data analysis made use of Glotaran software package.[51] The fs-TAS data were fit to a two-component sequential kinetic model.

2.2 Computational Methods

Geometry optimizations for the two possible tautomers of both molecules were performed in water and MeCN at the B3LYP/IEFPCM/6-311+g(d,p) level of theory.[52-54] The optimized structures were then used to perform single-point calculations at the MP2/IEFPCM[55] level of theory to obtain the relative energies between tautomers. All these calculations made use of the Gaussian 16 software package.[56] Minimum-energy structures, conical intersections, and crossing points of ThiaHX and ThiathioHX in the electronically excited and ground states were directly optimized by the complete active space second order perturbation theory (CASPT2) method[57-58] using the free OpenMolcas package.[59-60] In the geometry optimization, the cc-pVDZ basis sets[61] were used for all atoms without geometry constraints. The further single-point energy refinement of all the optimized structures was carried out with a larger cc-pVTZ basis set[61] together with the polarizable continuum model (PCM)[55] that is used to implicitly consider the solvation effects (acetonitrile). In all the CASPT2 calculations, the active space of 12 electrons in 10 orbitals was used. The Cholesky decomposition technique[62] for approximating two-electron integrals was employed; the electron ionization affinity (IPEA) shift[63] was set to zero and the imaginary shift technique (0.2 a.u.)[64] was carried out to avoid the issue of the intruder state. Excited state absorption spectra of the excited states were calculated in ORCA 4.2.1[65-66] using the expectation value formalism at TD-PBE0/CPCM/6-31+G(d,p)[54, 67-68] obtaining the first 20 transitions from the state of interest and convoluting the transitions with a Gaussian with FWHM of 75 nm.

3. Results

3.1. Steady-State Absorption and Emission Results

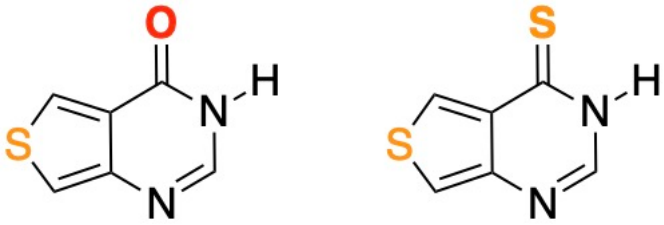

Scheme 1. Molecular structures of ThiaHX (left) and ThiathioHX (right). Note, while this heterocyclic system is numbered differently than the purine numbering, we will be using the latter nomenclature for familiarity and clarity throughout this study.

Figure 1 shows the absorption spectra of ThiaHX and ThiathioHX in phosphate buffer solution (PBS) at pH 7.4 and in MeCN. As observed for the canonical nucleobases,[15-16, 43] substitution of the oxygen atom of the carbonyl group by a sulfur atom at the C6 position results in a red shift of the lowest-energy absorption band from a maximum at 308 nm in ThiaHX in PBS to 367 nm in ThiathioHX (58 nm, 0.64 eV, or 5,145 cm^{-1}). An absorption tail that extends to ca. 430 nm is also observed in ThiathioHX, which is indicative of an nπ* transition. Remarkably, the molar absorption coefficient of the lowest-energy band maximum increases by 62% when going from ThiaHX to ThiathioHX (i.e., 4,400 ± 200 and 11,500 ± 300 M^{-1} cm^{-1} for ThiaHX and ThiathioHX, respectively). As observed in PBS, the absorption maximum of the lowest-energy absorption band of ThiaHX, now at 305 nm in MeCN, redshifts to 369 nm in ThiothiaHX and an absorption tail is also observed extending to ca. 450 nm. The absorption tail shifts to the red in going from PBS to MeCN, suggesting that the lowest-energy singlet state of ThiathioHX has nπ* character and is close in energy (i.e., overlap strongly) with the lowest-energy ππ* state. Similar than in PBS, the absorption coefficient of the lowest-energy band maximum increases significantly (i.e., 62%) when going from ThiaHX to ThiathioHX (i.e., 4,400 ± 200 and 11,600 ± 400 M^{-1} cm^{-1}) ThiaHX and ThiathioHX, respectively). Therefore, thionation of ThiaHX concurrently redshifts its lowest-energy absorption maxima by ca. 60 nm (5,145 cm^{-1}) and increases the absorption coefficient by 62% independent of the solvent, making ThiathioHX a significantly better absorber of near-visible radiation. In fact, using a typical absorption cross section cutoff of 1000 $M^{-1}cm^{-1}$,[13] ThiathioHX is expected to allow 18% deeper tissue penetration (up to ca. 100 μm) than 2,6-dithiopurine, one of the most promising thiobase PDT agents reported to date.[42]

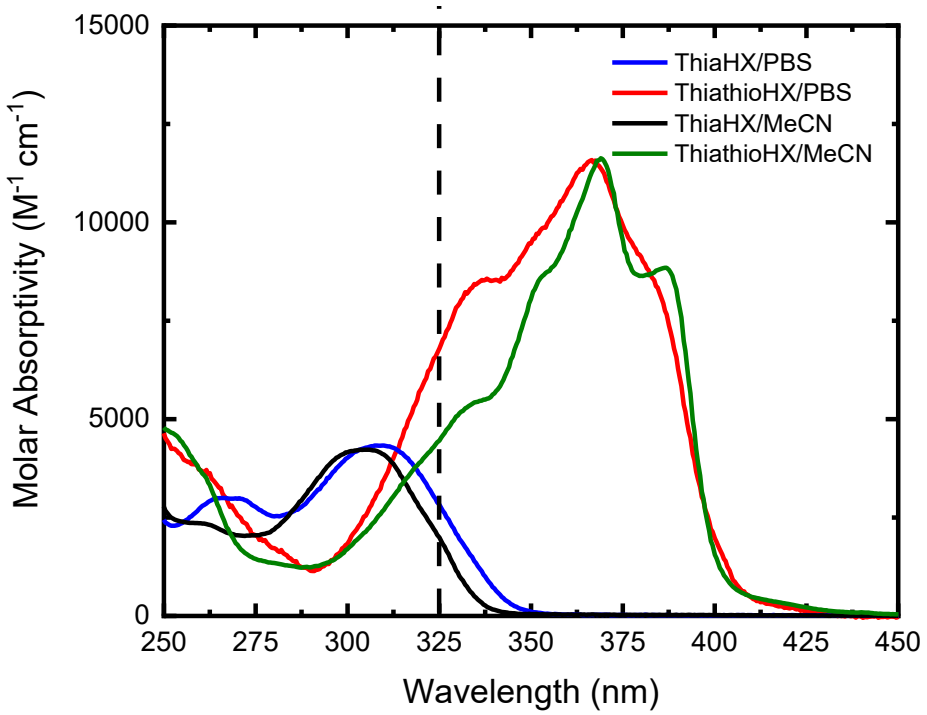

Figure 1. Absorption spectra of ThiaHX and ThiothiaHX in PBS at pH 7.4 and MeCN. The dashed, vertical line shows the excitation wavelength used in the transient absorption experiments of 325 nm.

Figure 2 depicts the emission spectra of ThiaHX in PBS at pH 7.4 and in MeCN. ThiaHX exhibits a relatively intense emission band with maximum at 386 nm in PBS and at 371 nm in MeCN. A fluorescence quantum yield of 0.31 ± 0.02 is measured in PBS, which is an order of magnitude higher than the one obtained in MeCN (0.028 ± 0.004). The blue shift of the emission band in going from PBS to MeCN is characteristic of an electronic transition with ππ* character. A E_{00} energy of 29,153 cm^{-1} (3.61 eV) and of 30,010 cm^{-1} (3.72 eV) was obtained from the crossing point of the normalized absorption and emission spectra of ThiaHX in PBS and in MeCN (Figure S1), respectively. In contrast, ThiathioHX does not exhibit any detectable emission in either solvent, demonstrating that most of the excited state population in ThiathioHX decays nonradiatively to the ground state or to a non-emissive excited state. In fact, the fluorescence quantum yields for both molecules are consistent with the observations from the steady-state absorption spectra, which suggest that the lowest-energy singlet state of ThiaHX should have ππ* character, while it should have nπ* character for ThiathioHX.

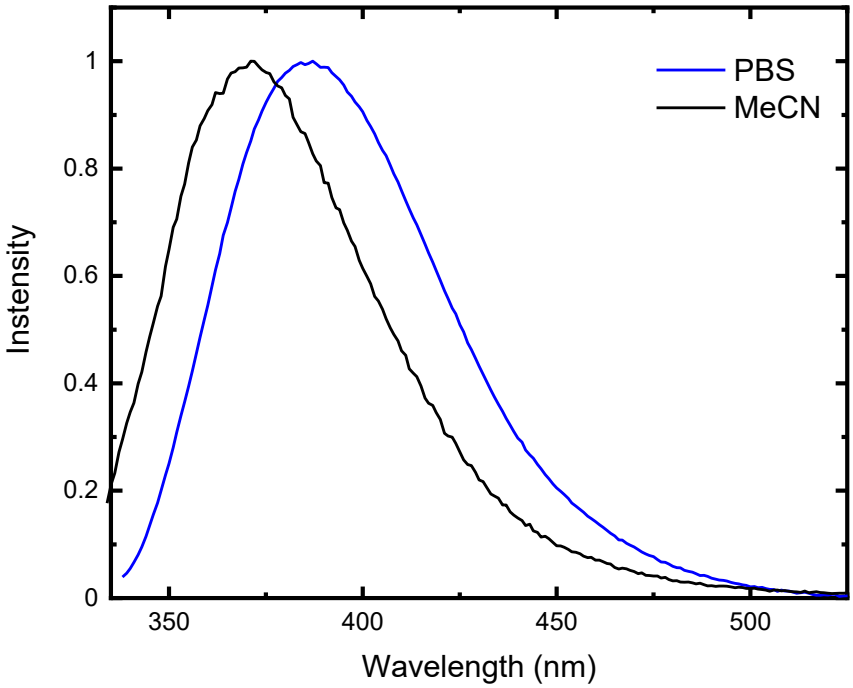

Figure 2. Normalized emission spectra of ThiaHX in PBS at pH 7.4 and in MeCN. Collection of the emission spectra of ThiathioHX in each solvent was attempted but no emission signal was detected.

3.2 Transient Absorption Results for ThiaHX

Figure 3 depicts the transient absorption spectra of ThiaHX in PBS at pH 7.4 and in MeCN upon excitation at 325 nm (3.81 eV). Initially, a transient species with absorption maxima at 360, 437, and 582 nm is observed in PBS within the cross-correlation of the pump and probe laser beams, which continues to grow up to a time delay of 0.6 ps (Figure 3a). The band with absorption maximum at 582 nm, however, continues to grow and blue shifts for up to 14 ps (Figure 3a). A depletion in excited state absorption is also observed around 390 nm, where the steady-state fluorescence of this thieno[3,4-d]pyrimidine derivative is observed (Figure 2). The transient species decays monotonically on a time scale longer than the 3 ns window reported in Figure 3b. Table 1 collects the lifetimes extracted from the global and target analysis of ThiaHX in PBS using a two-component sequential kinetic model, in which the second lifetime models the slow decay of the transient data in a time scale longer than 3 ns. Representative decay traces, best fits, and evolution-associated difference spectra (EADS) are shown in Figure 4a, c.

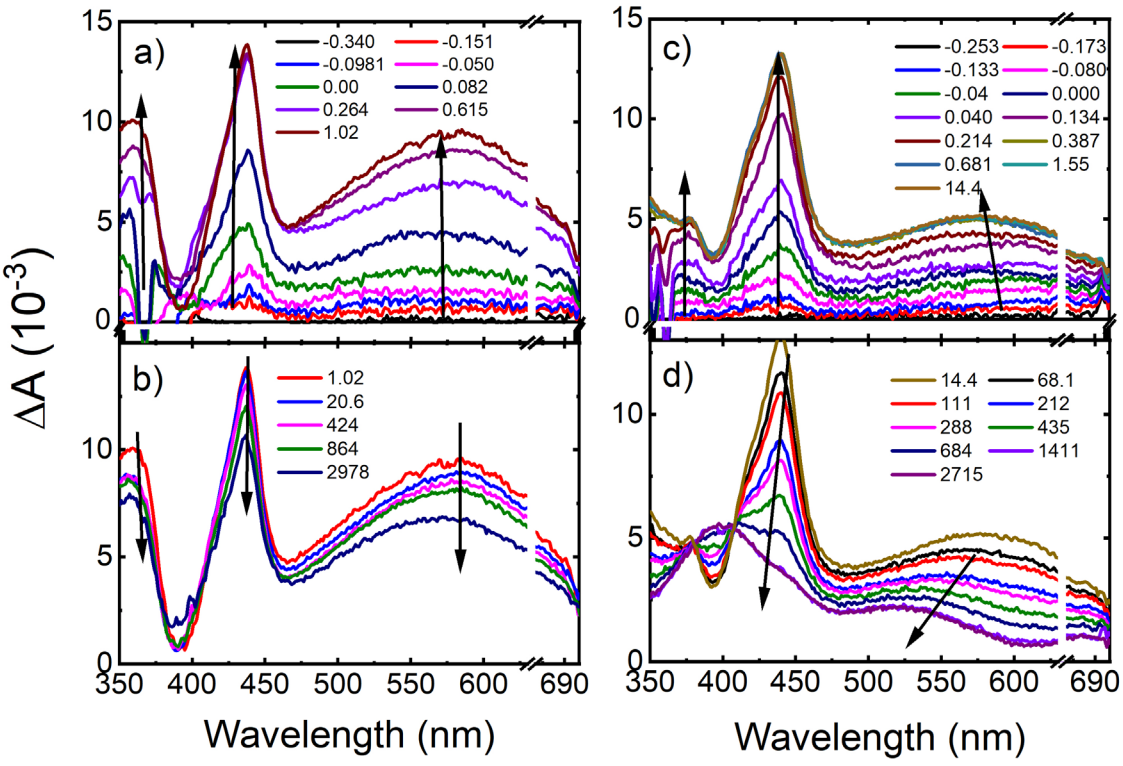

Figure 3. Transient absorption spectra of ThiaHX in PBS at pH 7.4 (a & b) and in MeCN (c & d) upon excitation with 325 nm. Stimulated Raman emission from the solvent is observed at 367 nm within the cross-correlation of the pump-probe beams. The breaks are covering the scattering of the pump and probe beams reaching the detectors.

Table 1. Lifetimes obtained from global analysis for ThiaHX and for ThiathioHX in PBS and MeCN upon excitation with 325 nm.

Lifetime	PBS	MeCN
ThiaHX (τ_1)	0.95 ± 0.04 fs	375 ± 20 ps
ThiaHX (τ_2)	> 3 ns (9 ns)*	> 3 ns (70 ns)*
ThiathioHX (τ_1)	1.2 ± 0.5 ps	9 ± 1 ps
ThiathioHX (τ_2)	> 3 ns (30 ns)*	> 3 ns (79 ns)*

* the value in parenthesis was obtained from the global and target analysis of the 3 ns time-resolved data.

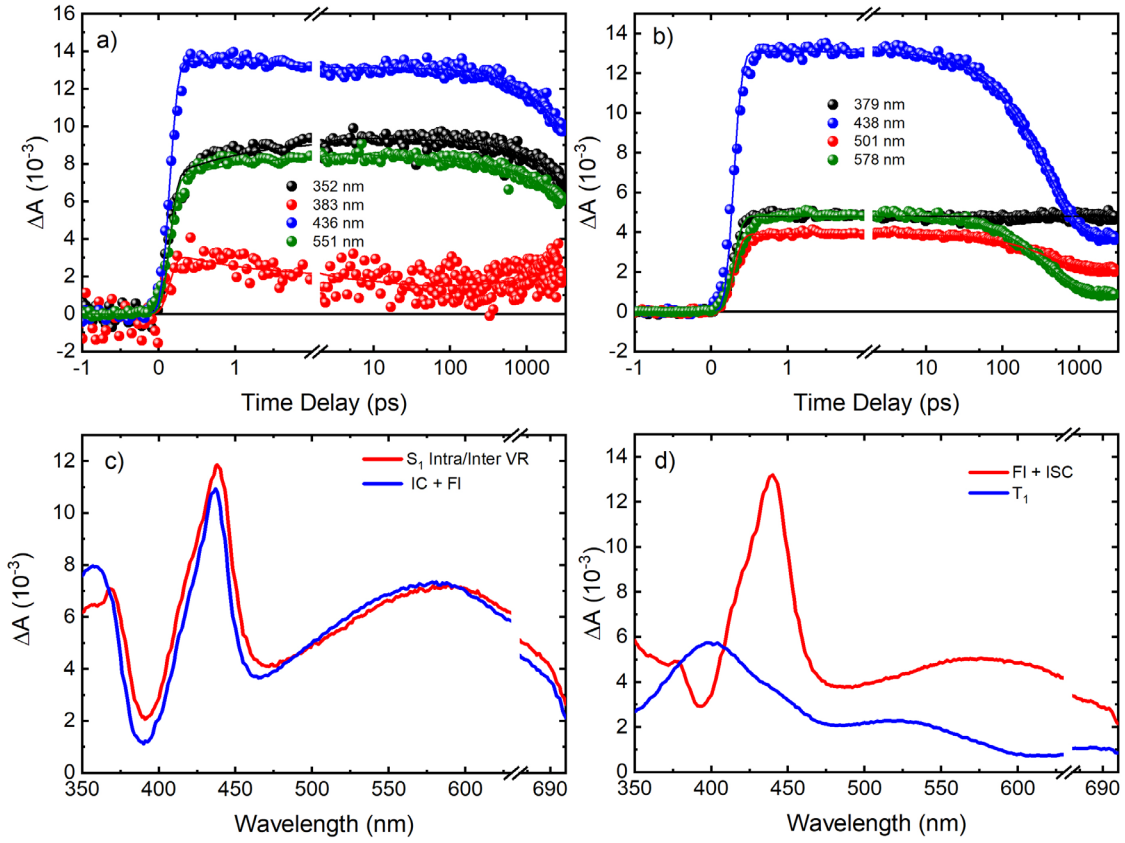

Figure 4. Decay Traces ThiaHX in a) PBS and in b) MeCN upon excitation with 325 nm. EADS of ThiaHX in c) PBS and in d) MeCN, extracted from the global and target analyses. VR, Fl, IC and ISC stand for vibrational redistribution, fluorescence, internal conversion, and intersystem crossing, respectively. The breaks are covering the scattering of the pump and probe beams reaching the detectors.

Figure 3 also depicts the fs-transient spectral evolution ThiaHX in MeCN upon excitation at 325 nm. A transient absorption species is populated within 14 ps, which has absorption band maxima at 376, 439, and 570 nm (Figure 3c). Additionally, the absorption band with maximum at 570 nm shows some blue shifting as it rises. Interestingly, a significant fraction of this transient species decays to populate another transient absorption species in hundreds of picoseconds, which has absorption maxima at ca. 400 and 530 nm (Figure 3d). Apparent isosbestic points are also observed at 377 and 407 nm, suggesting that indeed, the band with maxima at 400 and 530 nm corresponds to a new species. Table 1 collects the lifetimes extracted from the global and target analysis of ThiaHX in MeCN using a two-component sequential kinetic model, in which the second lifetime models the slow decay of the transient data in a time scale longer than 3 ns. Representative decay traces, best fits and evolution-associated difference spectra are shown in Figure 4b, d.

3.3 Transient Absorption Results for ThiathioHX

Figure 5 shows the transient absorption spectra of ThiathioHX in PBS at pH 7.4 upon excitation at 325 nm. A transient absorption band with maximum at shorter wavelengths than

450 nm rises and blue shifts within the cross-correlation of the pump and probe beams (Figure 5a). Ground state depopulation is also observed at wavelengths shorter than 400 nm. The absorption around 450 nm slightly blueshifts and increases its amplitude, while another absorption band simultaneously grow with maxima at 550 nm and around 400 nm (Figure 5b). An apparent isosbestic point is also observed at 510 nm, suggesting a state-to-state transition. From a delay time of 1 to 20 ps (Figure 5c), the transient species with absorption maximum around 400 nm starts to decay with a simultaneous increase of the ground-state depopulation signal at wavelengths shorter than 400 nm, while the absorption band with maximum around 550 nm redshift to ca. 565 nm. Additionally, a simultaneous increase in absorption at wavelengths larger than ca. 650 nm is observed for a delay time of up to 20 ps (Figure 5c), after which the transient species does not decay any further (Figure 5d) for up to 3 ns within experimental uncertainties. We remark that the apparent ground-state recovery observed during the first ca. 20 ps is possibly due to the population of transient species absorbing at wavelengths shorter than 450 nm and is not necessarily due to the repopulation of the ground state. Table 1 collects the lifetimes extracted from the global and target analysis of ThiathioHX in PBS using a two-component sequential kinetic model, in which the second lifetime models the slow decay of the transient data in a time delay much longer than 3 ns. Representative decay traces, best fits and evolution-associated difference spectra are shown in Figure 6a, c.

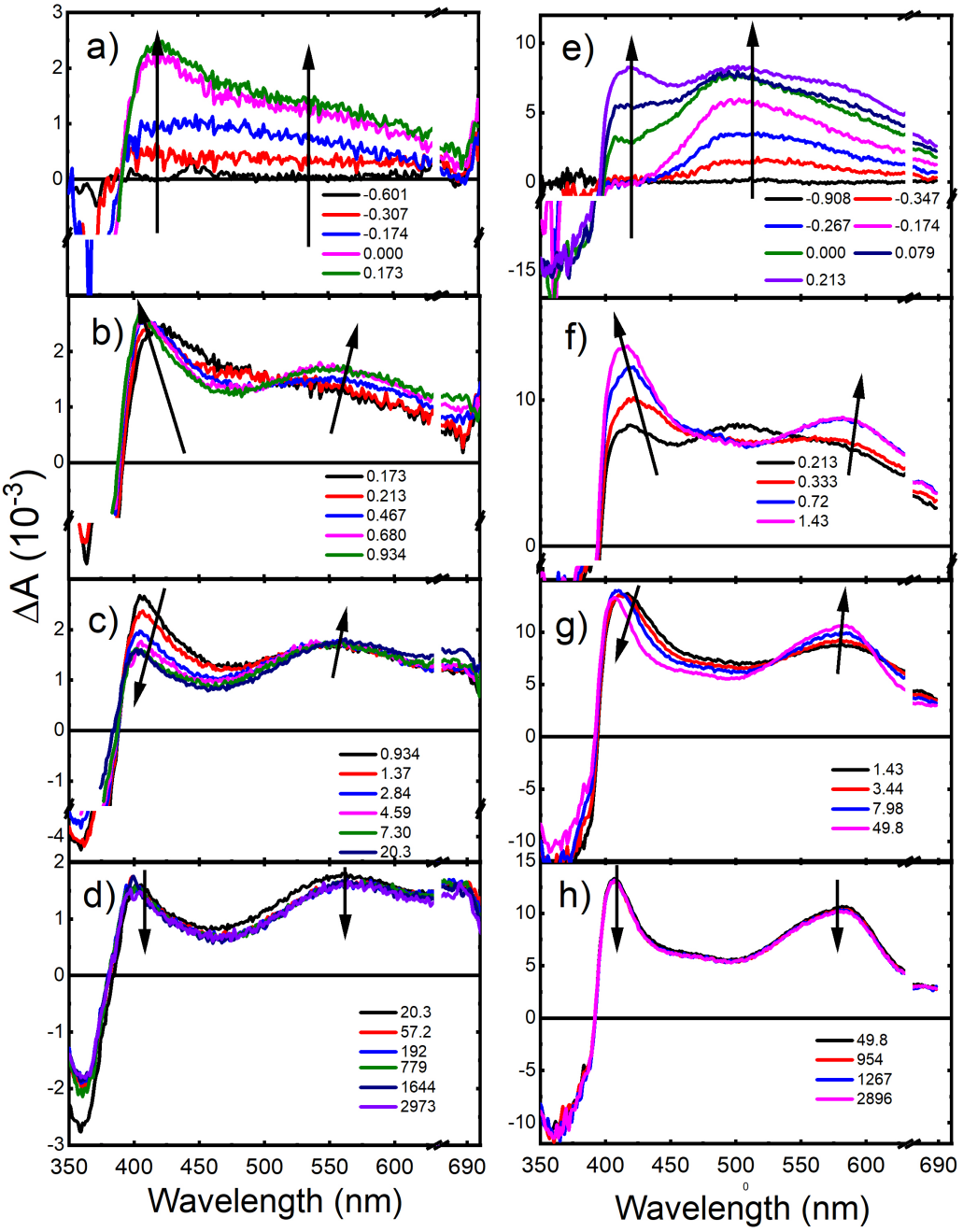

Figure 5. Transient absorption spectra of ThiathioHX in PBS at pH 7.4 (a-d) and MeCN (e-h) upon excitation at 325 nm. Stimulated Raman emission from the solvent is observed at 367 nm within the cross-correlation of the pump-probe beams. The breaks are covering the overtone of the pump beam at 650 nm.

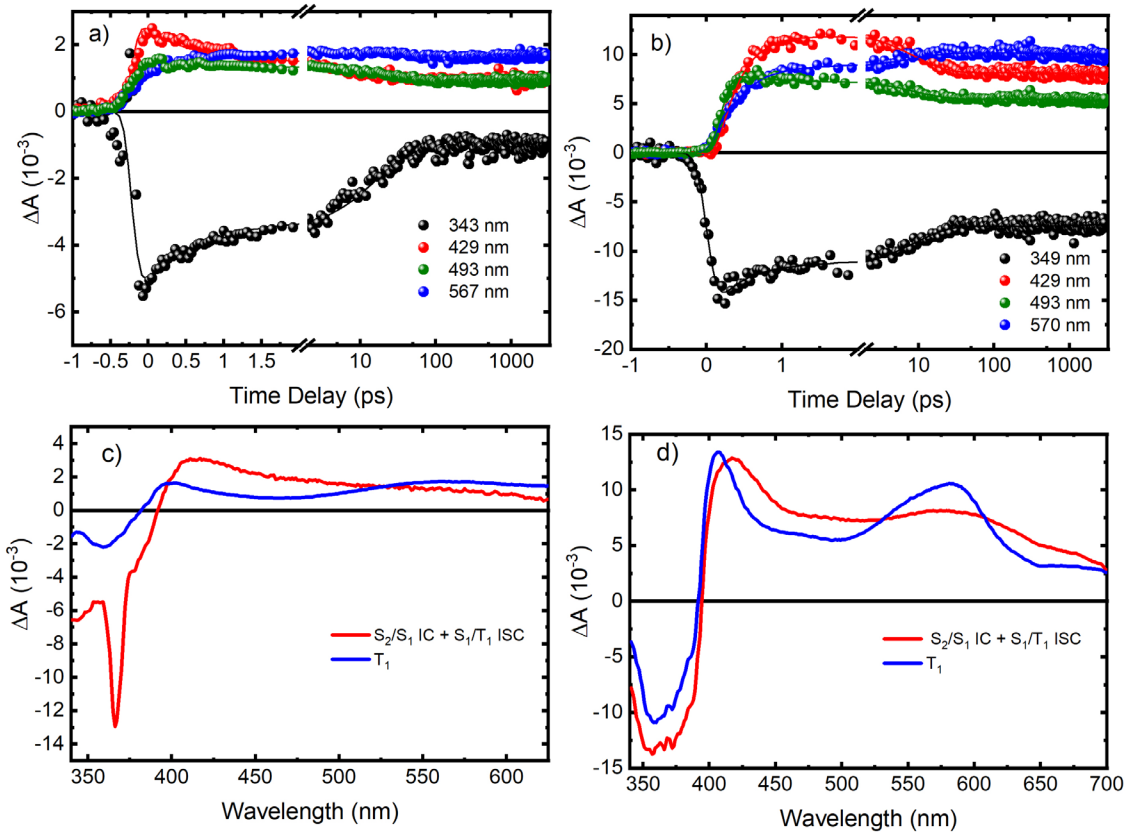

Figure 6. (a) Representative decay traces of ThiathioHX in PBS upon excitation with 325 nm and (b) EADS extracted from the global and target analyses.

In addition, Figures 5 shows the transient absorption results for ThiathioHX in MeCN exciting at 325 nm, while Table 1 reports the results from the target and global analyses. The formation of multiple bands with absorption around 420, 500, and 580 nm are observed during the initial 0.2 ps, which seems to be populated with different rates (Figure 5e). Additionally, the negative amplitude band observed below 400 nm is due to ground-state depopulation. The band with absorption maximum at 500 nm decays, while the bands with absorption maxima around 420 and 580 nm continue increasing for up to ca. 1.4 ps (Figure 5f). Apparent isosbestic points are also observed at 476 and 541 nm. From 1 to 50 ps (Figure 5g), the band with absorption around 420 nm blueshifts, while the band at 580 nm increases and redshifts. Additionally, the structure of the transient absorption band observed after 50 ps around 460 nm seems to be different than that of ThiathioHX in PBS. It is possible that more than one transient species is contributing to the overall transient absorption band. As observed in PBS, the ground-state depopulation signal slightly increases within these time delays and thus, we remark that the apparent ground-state recovery observed during the first ca. 50 ps is possibly due to the population of transient species absorbing at wavelengths shorter than 450 nm and not necessarily to the repopulation of the ground state. From 50 ps to 3 ns, the transient species do not decay significantly (Figure 5h). Representative decay traces, best fits and evolution-associated difference spectra are shown in Figure 6b, d.

3.4 Theoretical Results

To provide detailed and crucial electronic and nuclear information regarding the deactivation mechanisms of ThiaHX and ThiathioHX, quantum chemical calculations were performed. Based on the molecular structures of both thieno[3,4-d]pyrimidine derivatives, two possible tautomers may be expected to be available in solution, namely the N1(H) and N3(H) tautomers. Thus, to examine whether both tautomers are available in solution, ground-state optimizations were performed in water and MeCN at the B3LYP/IEFPCM/6-311+g(d,p) with subsequent single-point calculations at the MP2/IEFPCM level of theory. According to these calculations, the N1(H) tautomer is 6.3 and 6.4 kcal mol^{-1} more stable than the N3(H) tautomer in the case of ThiaHX in water and in MeCN, respectively (Figures S2 and S3). In the case of ThiathioHX, the N1(H) tautomer is 7.5 and 7.7 kcal mol^{-1} more stable than the N3(H) tautomer in water and in MeCN, respectively (Figures S2 and S3). These values are also in good agreement with the relative energies obtained between the tautomers for ThiaHX (5.4 kcal mol^{-1}) and ThiathioHX (8.8 kcal mol^{-1}) at the CASPT2/PCM/cc-pVTZ level of theory in MeCN, where the N1(H) is always the most stable tautomer (Figure S3). Therefore, we conclude that only the N1(H) tautomer of both ThiaHX and ThiathioHX is available in solution. In what follows, all the calculations presented were thus performed only for the N1(H) tautomer of both molecules.

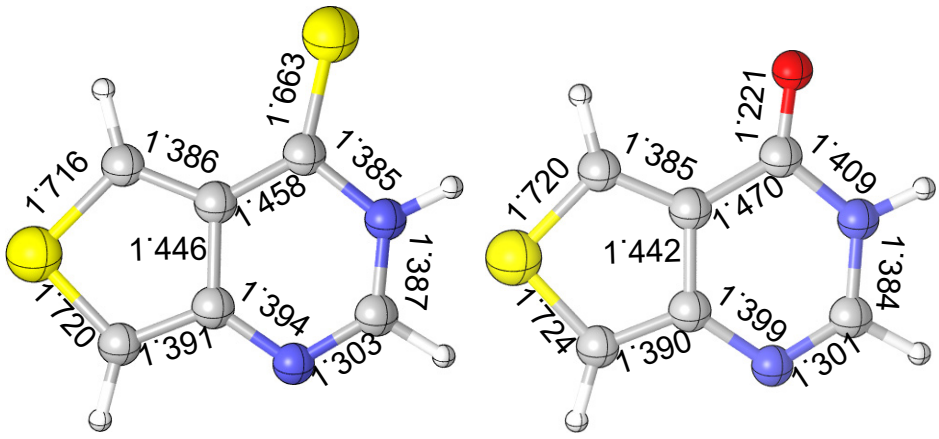

Figure 7. Ground-state optimized structures of ThiathioHX (left) and ThiaHX in MeCN obtained at the CASPT2/cc-pVDZ level of theory.

CASPT2 calculations were used to optimize the relevant ground- and excited-state structures, as shown in Figures 7, S6, and S9. Structurally, the thionation leads to significantly longer C=S bond lengths than the C=O counterparts in the S_0 state, e.g., 1.663 vs. 1.221 Å. Based on the optimized S_0 structures, the excited-state properties of ThiaHX and ThiathioHX at the Franck-Condon region have been explored. The first excited singlet state of ThiaHX has ππ* character, as judged by the relevant molecular orbitals and oscillator strength (Figure S4 and Table S1), and its vertical excitation energy is calculated to be 307 nm. These results are in good agreement with the experimental values of 308 and 305 in PBS and in MeCN, respectively. In contrast, the S_1 state of ThiathioHX is a spectroscopically dark state with nπ* character (oscillator strength of ca. 10^{-4}). The CASPT2 computed vertical

excitation energy of 447 nm is also close to the experimental values of ca. 430 nm in PBS and in MeCN. The S_2 state of ThiathioHX is an optically allowed ππ* state (Figure S5 and Table S2) and its excitation energy is predicted to be 374 nm. The predicted value is also close to the experimental values of 366 and 369 nm in PBS and in MeCN, respectively.

The emission properties were also explored at the CASPT2 level by optimizing the S_1 structures. For ThiaHX, the $S_1 \rightarrow S_0$ vertical emission is estimated to be 394 nm, with a reasonably large oscillator strength of 0.1. This theoretical estimation also agrees well with the experimental measurements of emission at 386 and 391 nm in PBS and in MeCN, respectively. For ThiathioHX, on the other hand, the S_1 state has nπ* character and the $S_1 \rightarrow S_0$ vertical emission is significantly weaker due to a negligible oscillator strength of ca. 10^{-5}. This satisfactorily explains why fluorescence emission is not detected for ThiathioHX in either PBS or MeCN (Figure 2). Furthermore, the adiabatic excitation energy of the S_1 state (i.e., the E_{00}) is estimated to be 29,519 cm^{-1} (3.66 eV) for ThiaHX and 21,615 cm^{-1} (2.68 eV) for ThiathioHX. The predicted values are in good agreement with those obtained experimentally for ThiaHX, 29,200 cm^{-1} (3.61 eV) and 30,000 cm^{-1} (3.72 eV) in PBS and in MeCN, respectively.

Figure 8 shows the CASPT2/PCM calculated order of the four lower energy electronic states for ThiaHX and the six lower energy electronic states for ThiathioHX. These electronic states are used to understand the excited-state relaxation pathways of ThiaHX and ThiathioHX in MeCN (see discussion section below). All relevant minima structures and linear interpolation of internal coordinates (LIIC) corresponding of the electronic states of ThiaHX are reported in Figure S7, while those of ThiathioHX are reported in Figures S8, respectively.

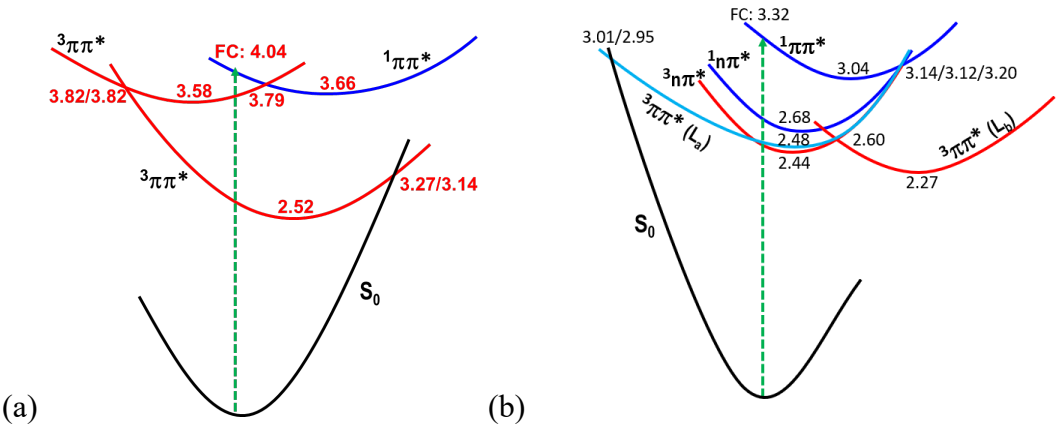

Figure 8. Proposed order of the four lower energy electronic states for ThiaHX (a) and the five lower energy states of ThiathioHX (b) in MeCN based on the calculations reported in this work. Values correspond to relative energies (in eV) of key stationary points, conical intersections, and crossing points.

When ThiaHX is excited to its $S_1(^1\pi\pi^*)$ state in the Franck-Condon region (4.04 eV), it is predicted to quickly relax to its excited state minimum, from which fluorescence emission can occur. During this process, there exists an $S_1(^1\pi\pi^*)/T_2(^3\pi\pi^*)$ crossing region, whose energy is only 0.13 eV higher than that of the $S_1(^1\pi\pi^*)$ minimum (3.66 eV). In addition, both

the $S_1(^1\pi\pi^*)$ and $T_2(^3\pi\pi^*)$ minima are nearly isoenergetic, 3.66 vs. 3.58 eV. Thus, the $S_1 \rightarrow T_2$ intersystem crossing process (ISC) is predicted to be energetically possible. However, because both excited states have $\pi\pi^*$ character, the corresponding S_1/T_2 spin-orbit coupling (SOC) is expected to be small according to the well-known EI-Sayed rule. This is supported by the calculated SOC value of 0.2 cm^{-1} at the S_1/T_2 crossing point (CASPT2/PCM level). If the $T_2(^3\pi\pi^*)$ state is populated, it will decay to the lower $T_1(^3\pi\pi^*)$ state in an ultrafast way via the T_2/T_1 conical intersection because such process only needs to overcome a barrier of 0.24 eV. In the $T_1(^3\pi\pi^*)$ state, the population is predicted to stay for a relatively long time because there is a large energy barrier separating the $T_1(^3\pi\pi^*)$ minimum and the $T_1(^3\pi\pi^*)/S_0$ crossing point. The energy barrier is calculated to be 0.75 eV relative to the T_1 minimum.

Conversely, according to the calculated vertical excitation energies for ThiathioHX, excitation at 325 nm populates directly the $S_2(^1\pi\pi^*)$ state at the Franck-Condon region (3.32 eV). Then, it is predicted to relax smoothly to its minimum, releasing 0.28 eV energy in the S_2 state. Importantly, in the vicinity of the S_2 minimum, there is an energetically accessible $S_2(^1\pi\pi^*)/S_1(^1n\pi^*)$ conical intersection, whose energy is only 0.1 eV higher than that of the S_2 minimum (see Figure S8b). Hence, the $S_2 \rightarrow S_1$ internal conversion process is predicted to occur efficiently and should become the dominant excited-state relaxation pathway for the population reaching the $S_2(^1\pi\pi^*)$ state. In addition to the $S_2 \rightarrow S_1$ internal conversion process, the $S_2(^1\pi\pi^*) \rightarrow T_2(^3n\pi^*)$ intersystem crossing pathway could play a role in the excited-state decay of the $S_2(^1\pi\pi^*)$ state. However, due to the relatively large energy gap between S_2 and T_2 in an extended region, the $S_2 \rightarrow T_2$ intersystem crossing process is not expected to be as efficient as the $S_2 \rightarrow S_1$ internal conversion process (see Figure S8). The population reaching the $S_1(^1n\pi^*)$ state, on the other hand, is predicted to intersystem cross to populate either the $T_2(^3n\pi^*)$ or the $T_3(^3\pi\pi^*, L_a)$ state. However, the $S_1 \rightarrow T_2$ intersystem crossing is not favorable considering the EI-Sayed rules because both excited states have $n\pi^*$ character and the corresponding SOC value is estimated to be 1.0 cm^{-1} at the CASPT2/PCM level. Instead, the $S_1(^1n\pi^*)$ state is expected to intersystem cross to populate the $T_3(^3\pi\pi^*, L_a)$ state because there is a small energy gap between them in a rather extended region (see Figure S8). Moreover, this intersystem crossing process is also facilitated by a relatively strong S_1/T_3 SOC of 91.2 cm^{-1}, as expected from the El-Sayed propensity rules.

According to the CASPT2/PCM calculations, there are two main nonradiative excited-state relaxation pathways that could occur from the $T_3(^3\pi\pi^*, L_a)$ state. In the first one, the system can evolve from the $T_3(^3\pi\pi^*, L_a)$ state into the energetically lower $T_1(^3\pi\pi^*, L_b)$ state after overcoming a small barrier of 0.12 eV at the CASPT2/PCM level of theory (see Figure S8d). In the second pathway, the system can decay to the S_0 state through the $T_1 \rightarrow S_0$ intersystem crossing process because the $T_3(^3\pi\pi^*, L_a)$ potential energy surface can cross the ground state at a T_3/S_0 crossing region. Nonetheless, this process needs to surmount an energy barrier of 0.53 eV at the CASPT2/PCM level. Overall, the evolution into the significantly more stable $T_1(^3\pi\pi^*, L_b)$ state should be preferred in MeCN. However, it should be remarked that the inter-conversion between both the $T_3(^3\pi\pi^*, L_a)$ and $T_1(^3\pi\pi^*, L_b)$ minima can proceed efficiently owing to the small energy difference and small associated barriers (Figure 8b).

Finally, in order to assist in the interpretation of the transient absorption data, the excited state absorption spectra of the $S_2(^1\pi\pi^*)$, $S_1(^1n\pi^*)$, $T_3(^3\pi\pi^*, L_a)$, $T_2(^3n\pi^*)$ and $T_1(^3\pi\pi^*, L_b)$

minima were calculated at the TD-PBE0/CPCM/6-31+G(d,p) level of theory in MeCN (Figure S10) using the structures calculated at the CASPT2(12,10)/cc-pVTZ/PCM level of theory.

4. Discussion

4.1 Electronic Relaxation Mechanism of ThiaHX upon Excitation at 325 nm

Understanding the electronic relaxation mechanisms of prospective PDT agents is essential to comprehend their photochemistry and to establish design principles to develop further derivatives that may exhibit optimal PDT properties. Given the experimental and theoretical results reported in the Results section, we are now in a favorable position to elucidate detailed electronic deactivation mechanisms for both thieno[3,4-d]pyrimidine derivatives. As described in Section 3.2, a transient species is initially populated within the cross-correlation of the pump and probe beams in ThiaHX. This transient species has absorption maxima at 360, 439, and 582 nm in PBS and at 376, 439 and 570 nm in MeCN (Figure 3a). The CASPT2/PCM calculations predict that the $S_1(^1\pi\pi^*)$ state is populated upon excitation at 325 nm. Taking these observations together, we assign the transient absorption species to the excited state absorption spectrum of the $S_1(^1\pi\pi^*)$ state. This assignment is also in agreement with the vertical excitation energies reported in Table S1.

In PBS, the transient band with absorption maximum at 582 nm continues to grow and blue shifts for up to 14 ps (Figure 3a). This is likely due to a combination of intra- and intermolecular vibrational redistribution of the excess energy in the $S_1(\pi\pi^*)$ state of ThiaHX. Thus, we assign the first lifetime to these processes. The observed transient absorption minimum around 390 nm is assigned to stimulated fluorescence emission from the $S_1(\pi\pi^*)$ state population, in agreement with the fluorescence emission band observed in Figure 2. The excited-state absorption spectrum of the $S_1(\pi\pi^*)$ state decays monotonically on a time scale longer than the 3 ns time window reported in Figure 3b. This is further supported by the fluorescence quantum yield of ca. 30% measured in this solvent. The need to include a second decay lifetime to model the transient data indicates that the fluorescence lifetime of ThiaHX is significantly longer than 3 ns. No evidence of the population of any other transient species is observed in Figure 3 when PBS is used as a solvent. Therefore, we propose that the excited state population in ThiaHX decays primarily back to the ground-state via a combination of nonradiative (internal conversion) and radiative (fluorescence) processes in PBS. This is in good agreement with the relatively high fluorescence quantum yield measured for this thieno[3,4-d]pyrimidine derivative in PBS (i.e., 0.31 ± 0.02). However, we cannot rule out whether a fraction of the 70% of the population that decays nonradiatively may intersystem cross to the triplet manifold at timescales longer than 3 ns or if it fully decays back to the ground state through internal conversion. Transient absorption experiments from nanoseconds to microseconds are required to answer this question. The proposed deactivation mechanism is shown in Scheme 2.

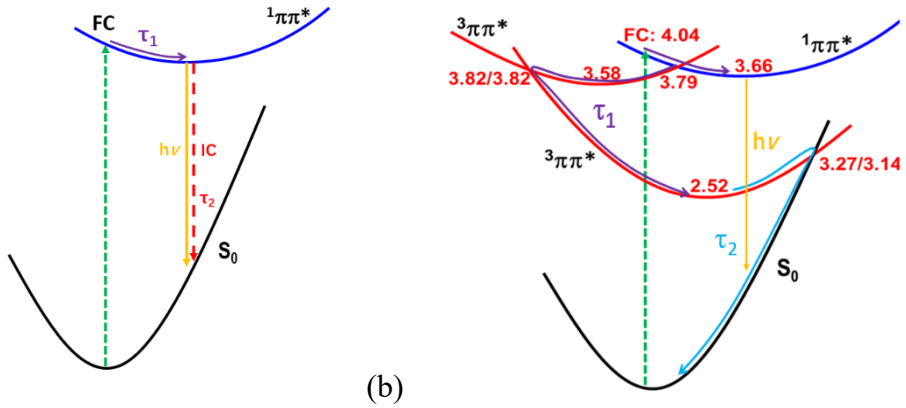

(a) (b)

Scheme 2. Proposed excited-state relaxation mechanisms for ThiaHX (a) in PBS and (b) in MeCN based on the calculations and experiments reported in this work. Values correspond to relative energies (in eV) of key stationary points, conical intersections, and crossing points. Note that in PBS only the $S_1 \rightarrow S_0$ internal conversion process and fluorescence are demonstrated to be relevant deactivation pathways for ThiaHX upon excitation at 325 nm.

Conversely, the population of an additional long-lived transient species is detected for ThiaHX in MeCN (Figure 3d). That another transient species is detected is supported by the observation of apparent isosbestic points at 377 and 407 nm and by the observation that the fluorescence quantum yield of ThiaHX in MeCN is an order of magnitude lower than in PBS. The latter observation further suggests that the transient species is not emissive. The CASPT2/PCM calculations predict that the population of the $S_1(^1\pi\pi^*)$ state can initially relax to a minimum in MeCN. The experimental data reported in Figure 3c confirm this process, where it can be observed that the band with maximum at 570 nm blueshifts. A blueshift of a transient absorption band is characteristic of intramolecular vibrational energy redistribution. Additionally, the calculations predict the existence of an $S_1(^1\pi\pi^*)/T_2(^3\pi\pi^*)$ crossing region, whose energy is only 0.13 eV higher than the energy of the $S_1(^1\pi\pi^*)$ minimum (3.66 eV). Furthermore, the energy of both $S_1(^1\pi\pi^*)$ and $T_2(^3\pi\pi^*)$ minima is nearly isoenergetic. The SOC at this crossing-region is small (i.e., 0.2 cm^{-1}) because both excited states have the same molecular orbital type, suggesting a relatively slow intersystem crossing pathway. The results of the calculations are consistent with the experimental observation of a state-to-state process in which a fraction of the $S_1(^1\pi\pi^*)$ state population intersystem crosses to populate the $T_2(^3\pi\pi^*)$ and/or $T_1(^3\pi\pi^*)$ state in hundreds of picoseconds. The population reaching the $T_2(^3\pi\pi^*)$ state will then decay to the lower $T_1(^3\pi\pi^*)$ state via a T_2/T_1 conical intersection region, because such process only needs to overcome a barrier of 0.24 eV (Figure 8). As consequence, the first lifetime obtained for ThiaHX in MeCN is assigned to a bifurcation process in which a fraction of the initial $S_1(^1\pi\pi^*)$ state population decays radiatively to the ground state, while another fraction intersystem crosses to the $T_2(^3\pi\pi^*)$ state through the $S_1(^1\pi\pi^*)/T_2(^3\pi\pi^*)$ crossing region. The population reaching the $T_2(^3\pi\pi^*)$ state internally converts in ultrafast time scale through a T_2/T_1 conical intersection to populate the $T_1(^3\pi\pi^*)$ state. Finally, the second lifetime is assigned to the decay of the $T_1(^3\pi\pi^*)$ state to the ground state, which occurs in a time scale much longer than 3 ns. The proposed relaxation mechanism is reported in Scheme 2b.

4.2 Electronic Relaxation Mechanism of ThiathioHX upon Excitation at 325 nm

Excitation of ThiathioHX at 325 nm results in the initial observation of a transient absorption species with maximum around ca. 450 nm in both solvents. This transient species rises and blueshifts within the cross-correlation of the pump and probe beams (Figure 5a), exhibiting an absorption maximum at shorter wavelengths than ca. 400 nm and a shoulder around 550 nm in PBS, while it exhibits absorption maxima around 420, 500 and 580 nm in MeCN. According to the calculated vertical excitation energies for ThiathioHX, excitation at 325 nm populates the $S_2(^1\pi\pi^*)$ state in the Franck-Condon (FC) region (3.32 eV), which can relax to its minimum releasing 0.28 eV of energy. Near the S_2 minimum, there is also an energetically accessible $S_2(^1\pi\pi^*)/S_1(^1n\pi^*)$ conical intersection that is close in energy to the S_2 minimum. Therefore, we propose that the initial transient signals observed upon excitation of ThiathioHX in both solvents corresponds to a combination of the population in the $S_2(^1\pi\pi^*)$ state, together with internal conversion through the $S_2(^1\pi\pi^*)/S_1(^1n\pi^*)$ conical intersection to the $S_1(^1n\pi^*)$ state. This assignment is in good agreement with the calculated excited state absorption spectra of the $S_2(^1\pi\pi^*)$ and $S_1(^1n\pi^*)$ reported in Figure S10. Furthermore, taking into consideration the results from the calculations, we also propose that in addition to the $S_2 \rightarrow S_1$ internal conversion process, a $S_2(^1\pi\pi^*) \rightarrow T_2(^3n\pi^*)$ intersystem crossing may also play a role in the relaxation of the $S_2(^1\pi\pi^*)$ state population. However, it should be remarked that because the energy gap is relatively large in an extended region between S_2 and T_2 potential energy surfaces, the $S_2 \rightarrow T_2$ intersystem crossing process is not expected to be as efficient as the $S_2 \rightarrow S_1$ internal conversion process, thus should only be playing a minor role.

The calculations also predict that the population reaching the $S_1(^1n\pi^*)$ state could undergo an intersystem crossing event to either populate the $T_2(^3n\pi^*)$ or the $T_3(^3\pi\pi^*)$ state. We expect that the $S_1 \rightarrow T_2$ intersystem crossing should play a minor role according to El-Sayed rules, while the $S_1 \rightarrow T_3$ pathway should play a major role in the intersystem crossing to the triplet manifold state in ThiathioHX. The calculations also predict that in addition to the $T_3(^3\pi\pi^*, L_a)$ a $T_1(^3\pi\pi^*, L_b)$ can be accessed in MeCN. We have calculated the excited state absorption spectra of both $T_3(^3\pi\pi^*, L_a)$ and $T_1(^3\pi\pi^*, L_b)$ minima in MeCN (Figure S10), and they are in good agreement with the transient species observed in the experimental transient absorption data. Specifically, the excited state absorption spectrum of the $T_1(^3\pi\pi^*, L_b)$ is in good agreement with the transient spectra observed in Figure 5d and the signal observed at 460 nm in Figure 5g,h is in good agreement with the excited state absorption spectrum of the $T_3(^3\pi\pi^*, L_a)$ (Figure S10). No evidence of the population of the $T_3(^3\pi\pi^*, L_a)$ minimum is observed in PBS. Hence, we propose that the long-lived transient species observed upon excitation of ThiathioHX with 325 nm corresponds to a combination of the $T_3(^3\pi\pi^*, L_a)$ and $T_1(^3\pi\pi^*, L_b)$ minima in MeCN, while it corresponds to the $T_1(^3\pi\pi^*, L_b)$ state in PBS. We propose that only the $T_1(^3\pi\pi^*, L_b)$ minimum is populated in PBS because the relative energy of the $T_3(^3\pi\pi^*, L_a)$ and $T_1(^3\pi\pi^*, L_b)$ minima significantly increase, making the $T_1(^3\pi\pi^*, L_b)$ the only $^3\pi\pi^*$ accessible for deactivation. Therefore, the apparent isosbestic point observed in the transient absorption spectra of ThiathioHX corresponds to the $S_1 \rightarrow T_1$ pathway in PBS and to the $S_1 \rightarrow T_3 \rightarrow T_1$ pathway in MeCN, and the ensuing transient absorption band corresponds to the excited state absorption of the long-lived $T_1(^3\pi\pi^*, L_b)$ state. Collectively, we propose that the first lifetime corresponds to a combination of the population of the $S_2(^1\pi\pi^*)$ state and internal conversion through the

$S_2(^1\pi\pi^*)/S_1(^1n\pi^*)$ conical intersection and intersystem crossing (i.e., $S_1 \rightarrow T_1$ in PBS and $S_1 \rightarrow T_3$ in MeCN). In MeCN, the first lifetime also encompasses the $T_3 \rightarrow T_1$ internal conversion. The second lifetime correspond to triplet decay. The proposed deactivation mechanism is reported in Scheme 3, which takes into consideration the experimental and computational results.

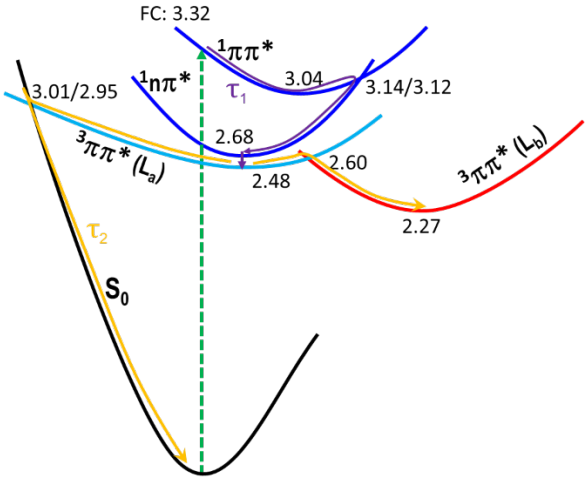

Scheme 3. Proposed excited-state relaxation mechanism for ThiathioHX in MeCN based on the experimental and computational results reported in this work. Values correspond to relative energies (in eV) of key stationary points, conical intersections, and crossing points in MeCN. In PBS, we propose that only the $T_1(^3\pi\pi^*, L_b)$ minimum is populated because the relative energy deference between the $T_3(^3\pi\pi^*, L_a)$ and $T_1(^3\pi\pi^*, L_b)$ minima increases, making the $T_1(^3\pi\pi^*, L_b)$ the only $^3\pi\pi^*$ accessible for deactivation.

Conclusions

In this study, we have demonstrated that thionation of thieno[3,4-d]pyrimidine derivatives affords the development of a potent all-organic HAF-Ps, thus, paving the way for the development of optimal photosensitizers based on the thionation of thieno[3,4-d]pyrimidine derivatives. Importantly, thieno[3,4-d]pyrimidine-4(1H)-thione stands out as the most promising heavy-atom-free, pyrimidine-based photosensitizer developed to this date. Like the thiobases,[16] these compounds can be readily incorporated in specific DNA and RNA sequences for targeting tumors and are expected to function as Trojan horses[16] both in the absence and in presence of molecular oxygen,[13, 15, 42, 44] facilitating more selective photodynamic therapy applications of skin cancer cells.

Specifically, we have investigated the electronic relaxation mechanisms of thieno[3,4-d]pyrimidin-4(1H)-one and of its thionated derivative in aqueous and acetonitrile solutions. Sulfur substitution in the carbonyl oxygen at the C6 position redshifts the lowest-energy absorption band of thieno[3,4-d]pyrimidin-4(1H)-one by about 60 nm (5,145 cm^{-1}), while simultaneously quenching its fluorescence and increasing its absorption coefficient by 62% independent of solvent. Irradiation of ThiathioHX at 400 or 410 nm should allow about 20% deeper tissue penetration (up to ca. 100 μm) than 2,6-dithiopurine or 4-thiothymidine, two of the most promising thiobase PDT agents reported to date.[12, 42] Thionation effectively alters the electronic relaxation mechanism of

thieno[3,4-d]pyrimidin-4(1H)-one, with a large fraction of the excited-state population decaying in an ultrafast time scale to populate the long-lived and reactive triplet state. Significantly, the intersystem crossing to the triplet state is independent of solvent environment, which is important in PDT, particularly when the photosensitizer is incorporated to cellular DNA or RNA. Conversely, fluorescence emission in thieno[3,4-d]pyrimidin-4(1H)-one is highly sensitive to solvent, with an order of magnitude decrease in fluorescence yield in going from aqueous to acetonitrile solution.

ASSOCIATED CONTENT

Supporting Information. Synthesis and analytical data, tables and figures with vertical excitation energies and oscillator strengths, computed main electronic configurations, ground-state relative energies, linearly interpolated internal coordinates paths, optimized excited state geometries, calculated excited state absorption spectra, and Cartesian coordinates of relevant geometries. This material is available free of charge via the Internet at http://pubs.acs.org/doi/.

AUTHOR INFORMATION

Corresponding Authors

* Dr. Carlos E. Crespo-Hernández,
E-mail: carlos.crespo@case.edu
ORCID: 0000-0002-3594-0890

* Dr. Yitzhak Tor,
E-mail: ytor@ucsd.edu

* Dr. Ganglong Cui,
E-mail: ganglong.cui@bnu.edu.cn

# these authors contributed equally to this work.

Notes

The authors declare no competing financial interest.

ACKNOWLEDGMENT

L.A.O-.R., and C.E.C.-H. acknowledge the National Science Foundation (Grant No. CHE-1800052). L.A.O-.R. also acknowledge the NSF-AGEP and the NOA-AGEP program for support. Y.T. thanks the National Institutes of Health for generous support (through grant GM 069773) and the Chemistry & Biochemistry MS and X-ray Facilities. G.C. thanks the National Natural Science Foundation of China (21688102). This work made use of the High Performance Computing Resource in the Core Facility for Advanced Research Computing at CWRU.

References

1. Morton, C. A.; Szeimies, R.-M.; Sidoroff, A.; Brathen, L. R., European guidelines for topical photodynamic therapy part 1: treatment delivery and current indications – actinic keratoses, Bowen's disease, basal cell carcinoma. *J. Eur. Acad. Dermatol. Venereol.* **2013,** *27*, 536-544.
2. Morton, C. A.; Szeimies, R.-M.; Basset-Seguin, N.; Calzavara-Pinton, P. G.; Gilaberte, Y.; Haedersdal, M.; Hofbauer, G. F. L.; Hunger, R. E.; Karrer, S.; Piaserico, S.; Ulrich, C.; Wennberg, A.-M.; Braathen, L. R., European Dermatology Forum guidelines on topical photodynamic therapy 2019 Part 1: treatment delivery and established indications – actinic keratoses, Bowen's disease and basal cell carcinomas. *J. Eur. Acad. Dermatol. Venereol.* **2019,** *13*, 2225-2238.
3. Morton, C. A.; Szeimies, R.-M.; Basset-Séguin, N.; Calzavara-Pinton, P. G.; Gilaberte, Y.; Haedersdal, M.; Hofbauer, G. F. L.; Hunger, R. E.; Karrer, S.; Piaserico, S.; Ulrich, C.; Wennberg, A.-M.; Braathen, L. R., European Dermatology Forum guidelines on topical photodynamic therapy 2019 Part 2: emerging indications – field cancerization, photorejuvenation and inflammatory/infective dermatoses. *J. Eur. Acad. Dermatol. Venereol.* **2020,** *34*, 17-29.
4. Allison, R. R.; Sibata, C. H., Oncologic photodynamic therapy photosensitizers: a clinical review. *Photodiagnosis Photodyn. Ther.* **2010,** *7*, 61-75.
5. Abrahamse, H.; Hamblin, Michael R., New photosensitizers for photodynamic therapy. *Biochem. J.* **2016,** *473*, 347-364.
6. Verhille, M.; Couleaud, P.; Vanderesse, R.; Brault, D.; Barberi-Heyob, M.; Frochot, C., Modulation of photosensitization processes for an improved targeted photodynamic therapy. *Curr. Med. Chem.* **2010,** *17*, 3925-3943.
7. Attili, S. K.; Dawe, R.; Ibbotson, S., A review of pain experienced during topical photodynamic therapy – our experience in Dundee. *Photodiagn. Photodyn. Ther.* **2011,** *8*, 53-57.
8. Bruijnincx, P. C. A.; Sadler, P. J., Controlling platinum, ruthenium, and osmium reactivity for anticancer drug design. *Adv. Inorg. Chem.* **2009,** *61*, 1-62.
9. Smith, N. A.; Sadler, P. J., Photoactivatable metal complexes: from theory to applications in biotechnology and medicine. *Phil. Trans. R. Soc. A* **2013,** *371*, 20120519.
10. Schmitt, F.; Govindaswamy, P.; Süss-Fink, G.; Ang, W. H.; Dyson, P. J.; Juillerat-Jeanneret, L.; Therrien, B., Ruthenium porphyrin compounds for photodynamic therapy of cancer. *J. Med. Chem.* **2008,** *51*, 1811-1816.
11. Monro, S.; Colón, K. L.; Yin, H.; Roque III, J.; Konda, P.; Gujar, S.; Thummel, R. P.; Lilge, L.; Cameron, C. G.; McFarland, S. A., Transition metal complexes and photodynamic therapy from a tumor-centered approach: challenges, opportunities, and highlights from the development of TLD1433. *Chem. Rev.* **2019,** *119*, 797-828.
12. Brem, R.; Guven, M.; Karran, P., Oxidatively-generated damage to DNA and proteins mediated by photosensitized UVA. *Free Radic. Biol. Med.* **2017,** *107*, 101-109.
13. Pollum, M.; Jockusch, S.; Crespo-Hernández, C. E., 2, 4-Dithiothymine as a potent UVA chemotherapeutic agent. *J. Am. Chem. Soc.* **2014,** *136*, 17930-17933.
14. Pollum, M.; Ashwood, B.; Jockusch, S.; Lam, M.; Crespo-Hernández, C. E., Unintended consequences of expanding the genetic alphabet. *J. Am. Chem. Soc.* **2016,** *138*, 11457-11460.

15. Ashwood, B.; Pollum, M.; Crespo-Hernández, C. E., Photochemical and photodynamical properties of sulfur-substituted nucleic acid bases. *Photochem. Photobiol.* **2019,** *95*, 33-58.
16. Ortiz-Rodríguez, L. A.; Crespo-Hernández, C. E., Thionated organic compounds as emerging heavy-atom-free photodynamic therapy agents. *Chem. Sic.* **2020,** *11*, 11113-11123.
17. Kamkaew, A.; Lim, S. H.; Lee, H. B.; Kiew, L. V.; Chung, L. Y.; Burgess, K., BODIPY dyes in photodynamic therapy. *Chem. Soc. Rev.* **2013,** *42*, 77-88.
18. Ortiz-Rodríguez, L. A.; Hoehn, S. J.; Loredo, A.; Wang, L.; Xiao, H.; Crespo-Hernández, C. E., Electronic relaxation pathways in heavy-atom-free photosensitizers absorbing near-infrared radiation and exhibiting high yields of singlet oxygen generation. *J. Am. Chem. Soc.* **2021,** *143*, 2676–2681.
19. Nguyen, V.-N.; Yan, Y.; Zhao, J.; Yoon, J., Heavy-atom-free photosensitizers: from molecular design to applications in the photodynamic therapy of cancer. *Acc. Chem. Res.* **2021,** *54*, 207-220.
20. Nguyen, V.-N.; Park, S. J.; Qi, S.; Ha, J.; Heo, S.; Yim, Y.; Baek, G.; Lim, C. S.; Lee, D. J.; Kim, H. M.; Yoon, J., Design and synthesis of efficient heavy-atom-free photosensitizers for photodynamic therapy of cancer. *Chem. Commun.* **2020,** *56*, 11489-11492.
21. Tang, J.; Wang, L.; Loredo, A.; Cole, C.; Xiao, H., Single-atom replacement as a general approach towards visible-light/near-infrared heavy-atom-free photosensitizers for photodynamic therapy. *Chem. Sci.* **2020,** *11*, 6701-6708.
22. Turkoglu, G.; Koygun, G. K.; Yurt, M. N. Z.; Demirok, N.; Erbas-Cakmak, S., Self-reporting heavy atom-free photodynamic therapy agents. *Org. Biomol. Chem.* **2020,** *18*, 9433-9437.
23. Buglak, A. A.; Charisiadis, A.; Sheehan, A.; Kingsbury, C. J.; Senge, M. O.; Filatov, M. A., Quantitative structure–property relationship modelling for the prediction of singlet oxygen generation by heavy-atom-free BODIPY photosensitizers. *Chem. Eur. J.* **2021**, https://doi.org/10.1002/chem.202100922.
24. Nguyen, V.-N.; Qi, S.; Kim, S.; Kwon, N.; Kim, G.; Yim, Y.; Park, S.; Yoon, J., An emerging molecular design approach to heavy-atom-free photosensitizers for enhanced photodynamic therapy under hypoxia. *J. Am. Chem. Soc.* **2019,** *141*, 16243-16248.
25. Kumar, P. P. P.; Yadav, P.; Shanavas, A.; Thurakkal, S.; Joseph, J.; Neelakandan, P. P., A three-component supramolecular nanocomposite as a heavy-atom-free photosensitizer. *Chem. Commun.* **2019,** *55*, 5623-5626.
26. Farrell, K. M.; Brister, M. M.; Pittelkow, M.; Sølling, T. I.; Crespo-Hernández, C. E., Heavy-atom-substituted nucleobases in photodynamic applications: substitution of sulfur with selenium in 6-thioguanine induces a remarkable increase in the rate of triplet decay in 6-selenoguanine. *J. Am. Chem. Soc.* **2018,** *140*, 11214-11218.
27. Luo, X.; Yang, Y.; Qian, X., Recent progresses on the development of thioxo-naphthalimides. *Chinese Chem. Lett.* **2020,** *31*, 2877-2883.
28. Wu, Y.; Zhu, W., Organic Sensitizers from D-π-A to D-A-π-A: effect of the internal electron-withdrawing units on molecular absorption, energy levels and photovoltaic performances. *Chem. Soc. Rev.* **2013,** *42*, 2039-2058.
29. Ravelli, D.; Fagnoni, M.; Albini, A., Photoorganocatalysis. What for? *Chem. Soc. Rev.* **2013,** *42*, 97-113.
30. Fukuzumi, S.; Ohkubo, K., Selective photocatalytic reactions with organic photocatalysts.

Chem. Sci. **2013,** *4*, 561-574.
31. Filatov, M. A., Heavy-atom-free BODIPY photosensitizers with intersystem crossing mediated by intramolecular photoinduced electron transfer. *Org. Biomol. Chem.* **2019,** *18*, 10-27.
32. Dong, Y.; Dick, B.; Zhao, J., Twisted bodipy derivative as a heavy-atom-free triplet photosensitizer showing strong absorption of yellow light, intersystem crossing, and a high-energy long-lived triplet state. *Org. Lett.* **2020,** *22*, 5535-5539.
33. Tang, J.; Robichaux, M. A.; Wu, K.-L.; Pei, J.; Nguyen, V.-N.; Zhou, Y.; Wensel, T. G.; Xiao, H., Single-atom fluorescence switch: a general approach toward visible-light-activated dyes for biological imaging. *J. Am. Chem. Soc.* **2019,** *141*, 14699-14706.
34. Brown, J. M.; Wilson, W. R., Exploiting tumour hypoxia in cancer treatment. *Nat. Rev. Cancer* **2004,** *4*, 437-447.
35. Wilson, W. R.; Hay, M. P., Targeting hypoxia in cancer therapy. *Nat. Rev. Cancer* **2011,** *11*, 393-410.
36. Höckel, M.; Vaupel, P., Tumor hypoxia: definitions and current clinical, biologic, and molecular aspects. *J. Nat. Cancer Inst.* **2001,** *93*, 266-276.
37. Vaupel, P.; Höckel, M.; Mayer, A., Detection and characterization of tumor hypoxia using pO_2 histography. *Antioxid. Redox Signal* **2007,** *9*, 1221-1236.
38. Massey, A.; Xu, Y.-Z.; Karran, P., Photoactivation of DNA thiobases as a potential novel therapeutic option. *Current Biol.* **2001,** *11*, 1142-1146.
39. Reelfs, O.; Karran, P.; Young, A. R., 4-Thiothymidine sensitization of DNA to UVA offers potential for a novel photochemotherapy. *Photochem. Photobio. Sci.* **2012,** *11*, 148-154.
40. Gemenetzidis, E.; Shavorskaya, O.; Xu, Y.-Z.; Trigiante, G., Topical 4-thiothymidine is a viable photosensitiser for the photodynamic therapy of skin malignancies. *J. Dermat. Treat.* **2013,** *24*, 209-214.
41. Pollum, M.; Guan, L.; Ahsanuddin, S.; Baron, E.; Lam, M.; Crespo-Hernández, C., Photoactivation of sulfur-modified DNA and RNA analogs induces cytotoxicity in epidermoid carcinoma cells. *J. Invest. Dermatol.* **2016,** *136*, S105.
42. Pollum, M.; Minh, L.; Jockusch, S.; Crespo-Hernández, C. E., Dithionated nucleobases as effective photodynamic agent against human epidermoid carcinoma cells. *ChemMedChem* **2018,** *13*, 1044-1050.
43. Pollum, M.; Martínez-Fernández, L.; Crespo-Hernández, C. E., Photochemistry of nucleic acid bases and their thio-and aza-analogues in solution. In *Photoinduced Phenomena in Nucleic Acids I*, Barbatti, M. B., A. C.; U. Susanne, Ed. Springer, Cham: Switzerland, 2015; Vol. 355, pp 245-327.
44. Ortiz-Rodríguez, L. A.; Reichardt, C.; Hoehn, S. J.; Jockusch, S.; Crespo-Hernández, C. E., Detection of the thietane precursor in the UVA formation of the DNA 6-4 photoadduct. *Nat. Commun.* **2020,** *11*, 3599.
45. Sholokh, M.; Sharma, R.; Shin, D.; Das, R.; Zaporozhets, O. A.; Tor, Y.; Mély, Y., Conquering 2-aminopurine's deficiencies: highly emissive isomorphic guanosine surrogate faithfully monitors guanosine conformation and dynamics in DNA. *J. Am. Chem. Soc.* **2015,** *137*, 3185-3188.
46. Rovira, A. R.; Fin, A.; Tor, Y., Expanding a fluorescent RNA alphabet: synthesis,

photophysics and utility of isothiazole-derived purine nucleoside surrogates. *Chem. Sci.* **2017,** *8*, 2983-2993.
47. Li, Y.; Fin, A.; McCoy, L.; Tor, Y., Polymerase-mediated site-specific incorporation of a synthetic fluorescent isomorphic G surrogate into RNA. *Angew. Chem. Int. Ed.* **2017,** *56*, 1303-1307.
48. Reichardt, C.; Vogt, R. A.; Crespo-Hernández, C. E., On the origin of ultrafast nonradiative transitions in nitro-PAHs: excited-state dynamics in 1-nitronaphthalene. *J. CHem. Phys.* **2009,** *131*, 224518.
49. Reichardt, C.; Wen, C.; Vogt, R. A.; Crespo-Hernández, C. E., Role of intersystem crossing in the fluorescence quenching of 2-aminopurine 2'-deoxyriboside in solution. *Photochem. Photobiol. Sci.* **2013,** *12*, 1341-1350.
50. Brister, M. M.; Crespo-Hernández, C. E., Excited-State Dynamics in the RNA Nucleotide Uridine 5'-Monophosphate Investigated using Femtosecond Broadband Transient Absorption Spectroscopy. *J. Phys. Chem. Lett.* **2019,** *10*, 2156-2161.
51. Snellenburg, J. J.; Laptenok, S.; Seger, R.; Mullen, K. M.; Van Stokkum, I., H. M., Glotaran: a Java-based graphical user interface for the R package TIMP. *J. Stat. Soft.* **2012,** *49*, 1-20.
52. Becke, A. D., A new mixing of hartree-fock and local density-functional theories. *J. Chem. Phys.* **1993,** *98*, 1372-1377.
53. Lee, C. T.; Yang, W. T.; Parr, R. G., Development of the colle-salvetti correlation-energy formula into a functional of the electron-density. *Phys. Rev. B* **1988,** *37*, 785-789.
54. Harihara.Pc;; Pople, J. A., Influence of polarization functions on molecular-orbital hydrogenation energies. *Theor. Chim. Acta* **1973,** *28*
213-222.
55. Miertus, S.; Scrocco, E.; Tomasi, J., Electrostatic interaction of a solute with a continuum - a direct utilization of abinitio molecular potentials for the prevision of solvent effects. *Chem. Phys.* **1981,** *55*, 117-129.
56. Frisch, M. J. T., G. W.; Schlegel, H. B.; Scuseria, G. E.; Robb, M. A.; Cheeseman, J. R.; Scalmani, G.; Barone, V.; Petersson, G. A.; Nakatsuji, H.; Li, X.; Caricato, M.; Marenich, A. V.; Bloino, J.; Janesko, B. G.; Gomperts, R.; Mennucci, B.; Hratch, D. J. *Gaussian 16 (Revision B.01)*, Gaussian, Inc.: Wallingford CT: Pittsburgh, PA, 2016.
57. Andersson, K.; Malmqvist, P. A.; Roos, B. O.; Sadlej, A. J.; Wolinski, K., 2nd-Order perturbation-theory with a CASSCF reference function. *J. Phys. Chem.* **1990,** *94*, 5483-5488.
58. Andersson, K.; Malmqvist, P. A.; Roos, B. O., 2nd-Order perturbation-theory with a complete active space self-consistent field reference function *J. Chem. Phys.* **1992,** *96*, 1218-1226.
59. Galvan, I. F.; Vacher, M.; Alavi, A.; Angeli, C.; Aquilante, F.; Autschbach, J.; Bao, J. J.; Bokarev, S. I.; Bogdanov, N. A.; Carlson, R. K.; Chibotaru, L. F.; Creutzberg, J.; Dattani, N.; Delcey, M. G.; Dong, S. S.; Dreuw, A.; Freitag, L.; Manuel Frutos, L.; Gagliardi, L.; Gendron, F.; Giussani, A.; Gonzalez, L.; Grell, G.; Guo, M.; Hoyer, C. E.; Johansson, M.; Keller, S.; Knecht, S.; Kovacevic, G.; Kallman, E.; Li Manni, G.; Lundberg, M.; Ma, Y.; Mai, S.; Malhado, J. P.; Malmqvist, P. A.; Marquetand, P.; Mewes, S. A.; Norell, J.; Olivucci, M.; Oppel, M.; Quan Manh, P.; Pierloot, K.; Plasser, F.; Reiher, M.; Sand, A. M.; Schapiro, I.; Sharma, P.; Stein, C. J.; Sorensen, L. K.; Truhlar, D. G.; Ugandi, M.; Ungur, L.; Valentini, A.;

Vancoillie, S.; Veryazov, V.; Weser, O.; Wesolowski, T. A.; Widmark, P.-O.; Wouters, S.; Zech, A.; Zobel, J. P.; Lindh, R., Open Molcas: from source code to insight. *J. Chem. Theory Comput.* **2019,** *15*, 5925-5964.
60. Aquilante, F.; Autschbach, J.; Baiardi, A.; Battaglia, S.; Borin, V. A.; Chibotaru, L. F.; Conti, I.; De Vico, L.; Delcey, M.; Galvan, I. F.; Ferre, N.; Freitag, L.; Garavelli, M.; Gong, X.; Knecht, S.; Larsson, E. D.; Lindh, R.; Lundberg, M.; Malmqvist, P. A.; Nenov, A.; Norell, J.; Odelius, M.; Olivucci, M.; Pedersen, T. B.; Pedraza-Gonzalez, L.; Phung, Q. M.; Pierloot, K.; Reiher, M.; Schapiro, I.; Segarra-Marti, J.; Segatta, F.; Seijo, L.; Sen, S.; Sergentu, D.-C.; Stein, C. J.; Ungur, L.; Vacher, M.; Valentini, A.; Veryazov, V., Modern quantum chemistry with Open Molcas. *J. Chem. Phys.* **2020,** *152*, 214117.
61. Dunning, T. H., Gaussian-Basis Sets for Use in Correlated Molecular Calculations .1. the Atoms Boron Through Neon and Hydrogen. *J. Chem. Phys.* **1989,** *90*, 1007-1023.
62. Aquilante, F.; Lindh, R.; Pedersen, T. B., Unbiased Auxiliary Basis Sets For Accurate Two-Electron Integral Approximations. *J. Chem. Phys.* **2007,** *127*, 114107.
63. Ghigo, G.; Roos, B. O.; Malmqvist, P. A., A Modified Definition of the Zeroth-Order Hamiltonian in Multiconfigurational Perturbation Theory (CASPT2). *Chem. Phys. Lett.* **2004,** *396*, 142-149.
64. Forsberg, N.; Malmqvist, P. A., Multiconfiguration Perturbation Theory with Imaginary Level Shift. *Chem. Phys. Lett.* **1997,** *274*, 196-204.
65. Neese, F., The ORCA program system. *Wiley Interdiscip. Rev. Comput. Mol. Sci.* **2012,** *2*, 73-78.
66. Neese, F., Software update: the ORCA program system, version 4.0. *Wiley Interdiscip. Rev. Comput. Mol. Sci.* **2018,** *8*, e1327.
67. Miertus, S.; Scrocco, E.; Tomasi, J., Electrostatic interaction of a solute with a continuum - a direct utilization of abinitio molecular potentials for the prevision of solvent effects. *Chem. Phys.* **1981,** *55*, 117-129.
68. Adamo, C.; Barone, V., Toward reliable density functional methods without adjustable parameters: The PBE0 model. *J. Chem. Phys. 110*, 6158-6170.

TOC

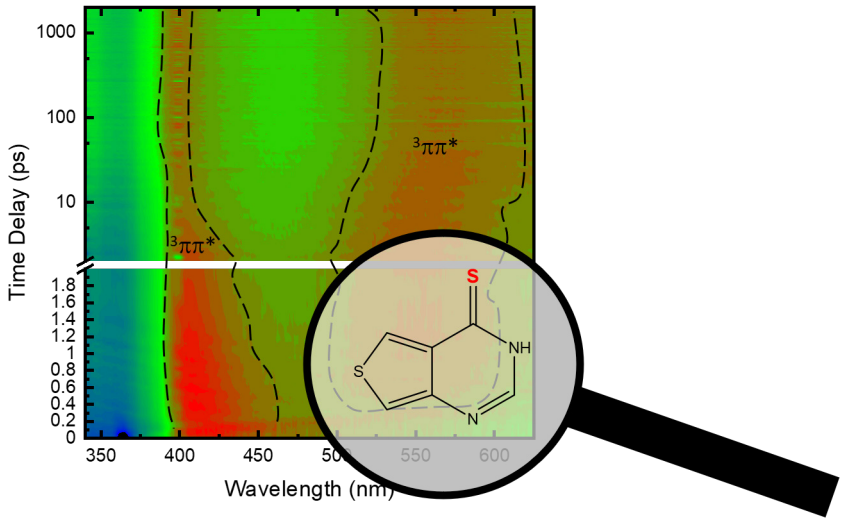
Time Delay (ps)
1000
100
10
1.8
1.6
1.4
1.2
1
0.8
0.6
0.4
0.2
0
350
400
450
550
600
Wavelength (nm)
$^3\pi\pi^*$
$^3\pi\pi^*$
S
NH
S
N